

Supplemental Material: Origin of the Counterintuitive Dynamic Charges in the Transition Metal Dichalcogenides

Nicholas A. Pike,^{1,*} Benoit Van Troeye,^{2,†} Antoine Dewandre,¹ Guido Petretto,² Xavier Gonze,² Gian-Marco Rignanese,² and Matthieu J. Verstraete¹

¹*nanomat/Q-Mat/CESAM, Université de Liège & European Theoretical Spectroscopy Facility, B-4000 Liège, Belgium*

²*Université Catholique de Louvain, Institute of Condensed Matter and Nanosciences (IMCN) & European Theoretical Spectroscopy Facility, B-1348 Louvain-la-Neuve, Belgium*

(Dated: May 5, 2017)

Our calculation and analysis of the Born Effective Charge (BEC) is outlined in the main text of the paper where we show that the BEC of the hexagonal Transition Metal Dichalcogenides (h-TMDs) have a counterintuitive sign, with the transition metal atom taking the negative charge and the chalcogen atoms the positive charge. In the present supplemental material, we present supporting information about these calculations and analysis to further emphasize the conclusions of the main text. We start by providing the details of the Density Functional Theory (DFT) and Density Functional Perturbation Theory (DFPT) calculations, then discuss the electronic screening contribution to the BEC calculation and show examples of the localized electric field response in the h-TMDs. Next, we show a projected band analysis detailing the atomic contributions to each molecular orbital, provide an analysis in terms of the change in the local polarization of the molecules, and then we compare our results for the BEC to the dynamic change of the Bader charge. Finally, we provide an example of the band-by-band decomposition of the BEC and further details about ways to experimentally confirm the sign of the BEC via measurement.

CALCULATION METHODS

As mentioned in the main text, our calculation uses Trouiller-Martins-type GGA-PBE pseudopotentials [1, 2] generated with the fhi98pp code for all atomic elements except W. For W we use a pseudopotential generated with the OPIUM code, which produce more accurate lattice parameters during our relaxation calculation. In addition to the exchange-correlation functional corresponding to the GGA-PBE pseudopotentials, we used a van der Waals (vdW) functional from Grimme [3], known as DFT-D3, to correctly model the long-range electron-electron correlations. Lattice parameters are determined using a Broyden-Fletcher-Goldfarb-Shanno minimization [4] and are summarized in Table S1. Throughout the calculation, several checks were made to ensure that the plane wave kinetic energy cut-offs (25 – 40 Ha) and electronic Brillouin zone sampling grid size ($8 \times 8 \times 8$ or $10 \times 10 \times 10$) were converged. Additionally, we use a ground state energy criteria of 1×10^{-10} Ha between

	$a(\text{\AA})$	$a^{\text{exp}}(\text{\AA})$	$c(\text{\AA})$	$c^{\text{exp}}(\text{\AA})$	Ref.
MoS ₂	3.162	3.160	12.301	12.290	[5]
MoSe ₂	3.287	3.287	13.003	12.919	[6]
MoTe ₂	3.496	3.519	13.895	13.964	[6]
WS ₂	3.155	3.153	12.398	12.167	[7]
WSe ₂	3.270	3.286	12.957	12.976	[8]
TiS ₂	3.478	3.410	5.749	5.690	[9]
TiSe ₂	3.639	3.533	6.180	5.995	[10]

TABLE S1. Lattice parameters of the bulk TMDs calculated within GGA-PBE and DFT-D3. The calculated lattice parameters are compared to experimental values.

changes of the self-consistent cycles and, for the vibrational properties, the variance of the ground state wavefunction and the first-order wavefunction were less than 1×10^{-18} and 1×10^{-10} . With these convergence parameters for the DFT calculation, we are able to compare our calculated lattice parameters to those found in the literature. This comparison indicates that our calculated lattice parameters agree to within 0.7% of the measured values.

ELECTRONIC SCREENING CONTRIBUTION TO THE BEC

Our calculation of the BEC comes from a mixed second derivative of the total energy with respect to an atomic displacement and an applied electric field. This mixed second derivative can be written as:

$$Z_{\kappa,\beta\alpha}^* = \frac{\partial^2 E}{\partial \mathcal{E}_\alpha \partial R_{\kappa\beta}} \quad (\text{S1})$$

which can be rewritten [11] into two terms as

$$Z_{\kappa,\beta\alpha}^* = Z_{\kappa,\beta\alpha}^{\text{ion}} + \Delta Z_{\kappa,\beta\alpha}. \quad (\text{S2})$$

The first term, Z_{κ}^{ion} , is the valence charge of the κ^{th} atom (6 for all elements considered here except W and Ti which have 16 and 4, respectively). The second term is due to the screening of an electric field perturbation by the electronic wave functions, and to the electronic potential change due to a displacement of an atom. Formally, the

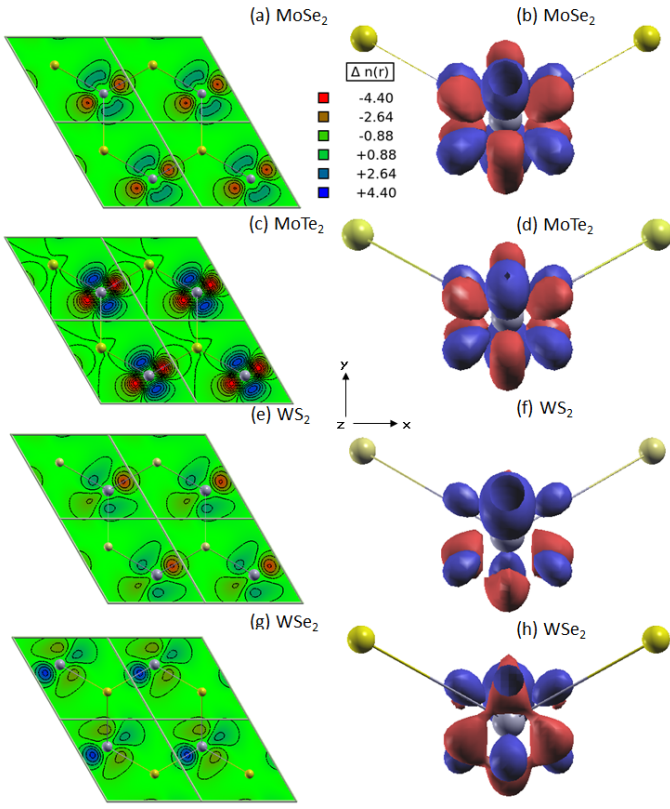


FIG. S1. (Color Online) Contour plots and isosurfaces of the change in the electronic density due to an electric field perturbation along the x axis for (a)-(b) MoSe_2 , (c)-(d) MoTe_2 , (e)-(f) WS_2 , and (g)-(h) WSe_2 . In each case, we show a contour plot of the change in electronic density taken through the transition metal ion and an isosurface for a single formula unit. Visualization provided by XcrySDen [12].

electronic screening term can be written as [11]

$$\Delta Z_{\kappa,\beta\alpha} = 2 \left(\frac{\Omega}{8\pi^3} \int_{BZ} \sum_m^{occ} s \langle u_{m\mathbf{k}}^0 | v_{sep,\mathbf{k},\mathbf{k}}^{R_{\kappa\alpha}} | u_{m\mathbf{k}}^{\mathcal{E}_\beta} \rangle d\mathbf{k} + \frac{1}{2} \int_{\Omega} \{ [v'_{loc,\mathbf{q}=0}(\mathbf{r}) + v_{xc0,\mathbf{q}=0}^{R_{\kappa\alpha}}(\mathbf{r})] [\bar{n}^{\mathcal{E}_\beta}(\mathbf{r})^*] \} d\mathbf{r} \right) \quad (S3)$$

where s is the spin degeneracy, Ω the unit cell volume, $|u_{m\mathbf{k}}^{0,\mathcal{E}_\beta}\rangle$ are the ground-state and first-order wave functions, $\bar{n}^{\mathcal{E}_\beta}(\mathbf{r})^*$ is the change in the electron density due to the electric field perturbation in the β^{th} direction. The potentials, v , are the non-local potential, local potential, and exchange-correlation potential defined in Ref. 13.

From Eq. (S3) we see that there are two primary contributions to the calculated BEC. The first is the change of the wave functions due to an electric field perturbation (i.e. the electron density) and the second is the electronic potential due to an atomic displacement. As outlined in the main text, the effect of the electric field perturbation in these systems is unique and leads to the observed sign

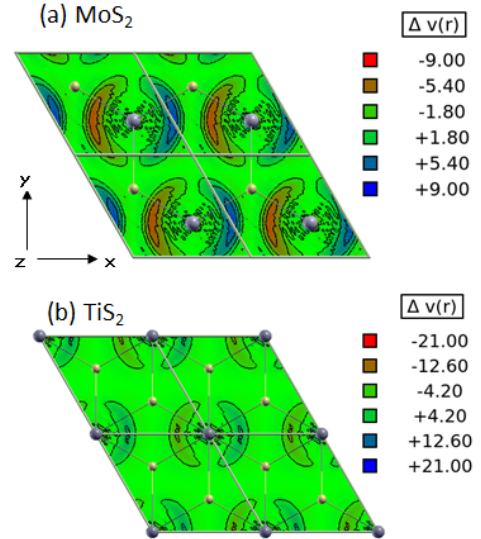


FIG. S2. (Color Online) Contour plots, in the xy plane through the transition metal ion, of the change in the electronic potential due to a change in the atomic position of the metal atom along the x direction for a single unit cell of (a) MoS_2 and (b) TiS_2 . Visualization provided by XcrySDen [12].

inversion of the BEC. We have already shown the change in the electron density for MoS_2 in the main text. In what follows, we show the change for the other h-TMDs, which display very similar characteristics.

ANALYSIS OF THE CHANGE IN THE ELECTRONIC DENSITY AND ELECTRONIC POTENTIAL

As part of the analysis of Eq. (S3) we investigate the changes in the electronic density due to an electric field perturbation. As mentioned in the main text, for the h-TMDs we find no change in the electron density around the chalcogen atom and only find a localized response near the transition metal ion. In Fig. S1 we show the change in the electronic density due to an electric field perturbation along x -axis for MoSe_2 , MoTe_2 , WS_2 , and WSe_2 in which red indicates a negative change, blue corresponds to a positive change, and green indicates approximately no change in the electronic density. In each case, we find a localized change in the electronic density around the transition metal ion, with slightly different shapes, less symmetric for W.

In Fig. S2 we show a contour plot, in the xy plane through the transition metal atom, of the change in the electronic potential for (a) MoS_2 and (b) TiS_2 due to an atomic displacement of the transition metal ion. Red indicates a negative change in the potential, blue corresponds to a positive change, and green indicates no change in the electronic potential. We find in both compounds that the change in the electronic potential around

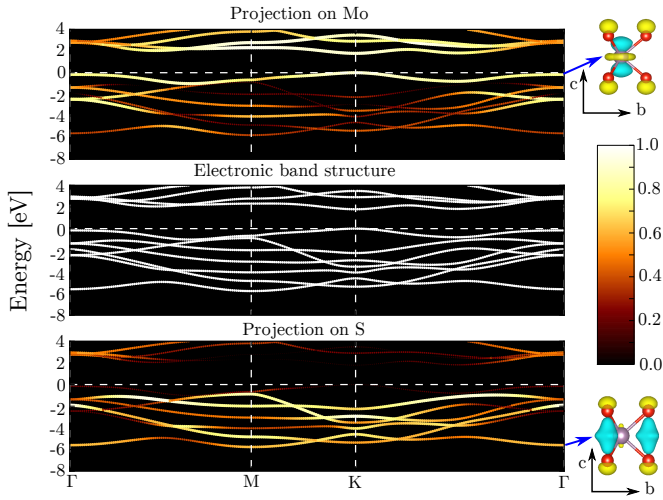


FIG. S3. (Color Online) Atomic projections of the electronic band structure of monolayer MoS₂. The top panel corresponds to a projection onto the atomic orbitals of Mo and the bottom graph corresponds to a projection onto the atomic orbitals of S. The middle plot corresponds to the standard electronic band structure of monolayer MoS₂. An isosurface of the real part of the wavefunction at the zone-center is shown to the right for the bonding or antibonding character of band indicated by the arrow. Yellow indicates a positive value for the wavefunction and blue a negative value.

the transition metal is similar and symmetric and the change around S is negligible.

PROJECTED BAND ANALYSIS

In order to investigate the origin of the localized change in polarization around the transition metal ion in h-TMDs, and in order to validate the molecular orbital diagrams presented in the main text of the paper, we have compared the projected electronic band structures of MoS₂ and TiS₂. The weight associated with a given atomic species is normalized such that the sum over the weights of all the atoms is equal to one for any k-point and band (i.e. we ignore interstitial contributions). The calculations are performed within the PAW formalism [14, 15], with a GGA-PBE exchange-correlation functional and the corresponding JTH pseudopotentials [16, 17]. We work in the PAW formalism for these projected band analyses to avoid the ambiguity of the projected sphere radii. Here we simply use the PAW augmentation radii as the projected sphere radii. A plane-wave cut-off energy of 15 Ha for the main grid and of 30 Ha for the auxiliary grid are found sufficient for convergence purposes. We use the geometries found within the norm-conserving approximation.

In order to simplify the analysis, we start by presenting results for monolayer MoS₂. While the global conclusions

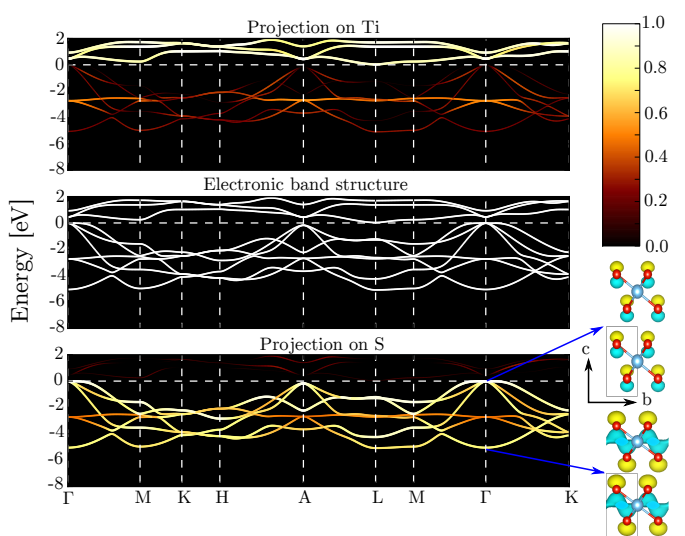


FIG. S4. (Color Online) Atomic projections of the electronic band structure of bulk TiS₂. The top panel corresponds to a projection onto the atomic orbitals of Ti and the bottom graph corresponds to a projection onto the atomic orbitals of S. The middle plot corresponds to a standard calculation of the electronic band structure. Isosurfaces of the real part of the wave function at the zone-center for the last occupied state and of the imaginary part of the wavefunction for the lowest-energy state are shown to indicate the character of the corresponding electronic states. The gray box represents the unit cell. Yellow indicates positive value for the real (imaginary) part of the wavefunction and blue a negative value.

are the same for the monolayer and the bulk, the doubling of the number of atoms per unit cell (due to the AB stacking) and the lifting of degeneracies, due to the interaction between the layers, make the comparison less immediate for the bulk. The stacking of bulk TiS₂ is simply AA and shows little difference with respect to monolayers. The atomic projections for monolayer MoS₂ and for bulk TiS₂ are shown in Figs. S3 and S4, respectively. We show in the top panel the projection of the wave function on the transition metal atomic orbitals; in the middle panel, the “standard” electronic band structure; in the bottom panel, the projection of the wave function on the chalcogen orbitals. The atomic projection for monolayer MoS₂ corresponds well to the Molecular Orbital diagrams presented in the main text. Indeed, in terms of relative weight of Mo and S, we find mixed character for most of the bands, except for the last occupied band, which is mostly of Mo character.

For the trigonal Transition Metal Dichalcogenide (t-TMD) TiS₂, the valence bands are primarily chalcogen in nature (see bottom panel of Fig. S4) and the conduction bands are almost entirely transition metal in character (top panel of Fig. S4). To highlight the difference in the atomic nature of the last occupied band and the others, we depict the real part of the wavefunction (or imaginary

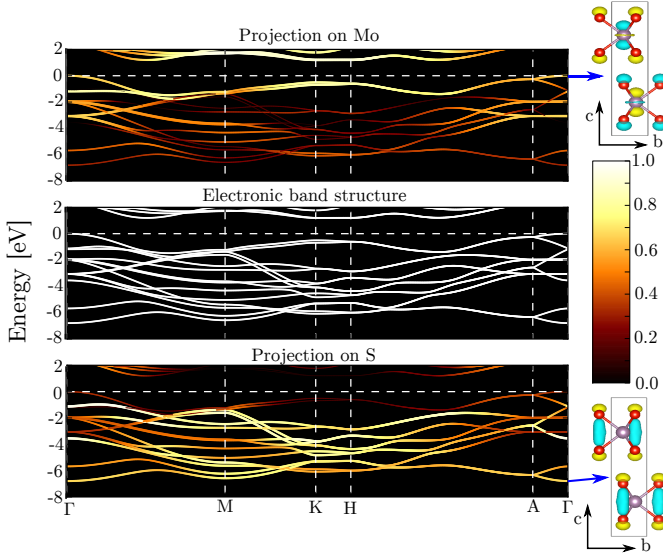


FIG. S5. (Color Online) Atomic projections of the electronic band structure of bulk MoS₂. The top panel corresponds to a projection onto the atomic orbitals of Mo and the bottom graph corresponds to a projection onto the atomic orbitals of S. The middle plot corresponds to a standard calculation of the electronic band structure. An isosurface of the real part of the wave function at the zone-center is shown to the right for the bonding or antibonding character of the band indicated by the arrow. The gray box represents the unit cell. Yellow indicates positive value for the real part of the wavefunction and blue a negative value.

part when this real part is zero) at the zone-center for both cases in the bottom right corner of Figs. S3 and S4. While the last occupied band is clearly antibonding in MoS₂ (no sharing of e⁻ between Mo and S), the other occupied orbitals are bonding orbitals, where both Mo and S share electrons. In the case of TiS₂, the isosurface of the wave function reveal that the situation is quite different: the last occupied orbital does not involve Ti orbitals and corresponds simply to the S-S non-bonding orbital. This stark difference in the projected band structure holds for all the h-TMDs.

Finally, we show the atomic projection for bulk MoS₂ in Fig. S5, with the real part of the wavefunction for the last occupied band and the lowest-energy state as for the monolayer case in Fig. S3. The picture is similar to the case of the monolayer i.e. the last two occupied orbitals are antibonding, with a slight lifting of degeneracy with respect to the monolayer, which indicates the weak interaction between the layers.

BADER PARTITIONED DYNAMICAL CHARGES

As discussed in the main text, the Bader definition of charge is static and determined by a partition of the electronic density using both the valence and core charge,

while the BEC is a dynamic charge, corresponding to the response of the system to a given perturbation. Therefore, they cannot be directly compared as they simply do not express the same physics. In order to compare them, one has to construct a dynamic charge based on the Bader partitioning. This newly-constructed charge can be then compared directly to the BEC, and therefore allow us to accurately determine the origin of the counterintuitive sign of these last charges.

Following the work of Ghosez and Gonze [11], we express the polarization of a given system P_α as a sum of the atomic positions of the atoms, $R_{\kappa'\alpha}$, times their charge $Z_{\kappa'}^B$ (here determined using both the valence and core charge) as:

$$P_\alpha = \sum_{\kappa'} Z_{\kappa'}^B R_{\kappa'\alpha}. \quad (S4)$$

The dynamical charge for such a system, expressed as the change in polarization due to an atomic displacement, is

$$\begin{aligned} Z_{\kappa\beta,\alpha}^{B,*} &= \frac{\partial P_\alpha}{\partial R_{\kappa\beta}} = \frac{\partial (\sum_{\kappa'} Z_{\kappa'}^B R_{\kappa'\alpha})}{\partial R_{\kappa\beta}} \\ &= Z_\kappa^B \delta_{\kappa\kappa'} \delta_{\alpha\beta} + \sum_{\kappa'} R_{\kappa'\alpha} \frac{\partial Z_{\kappa'}^B}{\partial R_{\kappa\beta}}. \end{aligned} \quad (S5)$$

Thus, the Bader Partitioned Dynamic Charge (BPDC) is composed of (1) the Bader charge of the atom in question and (2) the change of all of the Bader charges when the atom is moved. This second term includes the effects of charge (de)localization, which are impossible to account for in static charges. We estimate this dynamic contribution by finite differences for bulk MoS₂, displacing the Mo atom in the z direction with respect to its equilibrium position.

In Fig. S6, we show the change of the Bader charges as a function of the displacement of the Mo atom in the upper layer of the MoS₂ unit cell, along the \hat{x} [panels (a) and (b)] and the \hat{z} [panel (c) and (d)] directions. For the in-plane displacement, one can see that this induces a change of charge in the lower layer of the same magnitude as in the upper one. This change is associated with the creation of an electron current [11], whose contribution to the dynamical charge appears as an integrated effect in this approach. In contrast, for a displacement out-of-plane, the change of charge for the lower layer is one order of magnitude smaller. In this case, the response is local (no electron current) and we analyze it further.

The BPDCs, computed with the method described above, are presented in Table I of the main text. In TiS₂, the dynamical contribution is found to be too small to explain the sign of the Born effective charge. As it will be shown in the next section, this is due to the local change of polarization close to the Mo atoms, that cannot be accounted for by the finite difference Bader approach. The same development has been performed for the other h-TMDs and for TiSe₂ (not shown) with similar results.

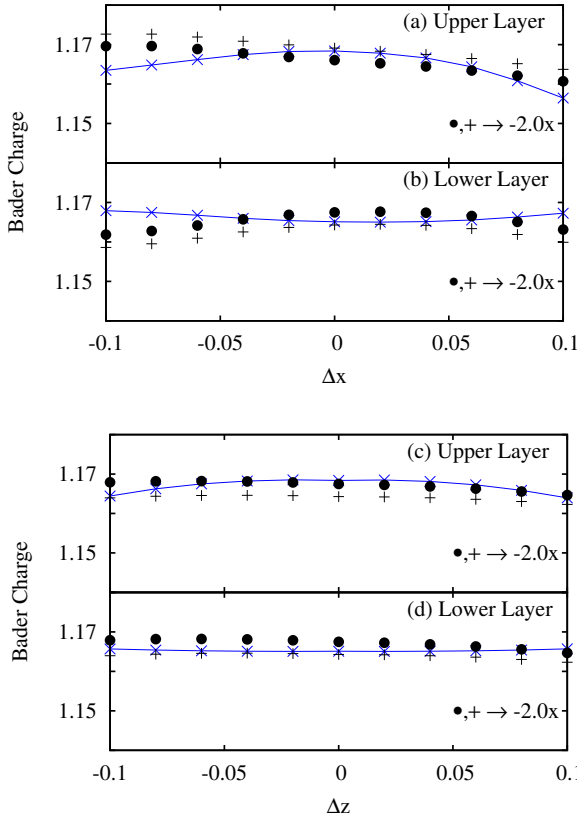


FIG. S6. (Color Online) Calculated Bader charge as a function of the change in the x (upper panel) or z (lower panel) coordinates (in Bohr) of the Mo atom in the upper layer of the unit cell of MoS_2 . (a) and (c) the Bader charges for the atoms in the upper layer and (b) and (d) the Bader charges for the atoms in the lower layer. The blue line corresponds to the Bader charge of Mo and the two sets of black points correspond to the charges of the two neighboring S atoms (multiplied by -2.0). The black dots and plus symbols correspond to the S atoms above and below Mo.

CHARGE LOCALIZATION

In order to investigate the fundamental differences between the BEC and the BPDC, we developed a real space approach based on the definition of these charges. It will be shown that the main contribution to the BEC is localized around the Mo atom, a region that, as it will be demonstrated, cannot be described by the BPDC. For this purpose, we derive several mathematical expressions that connect the BEC and the BPDC in term of comparable real-space variables.

Born Effective Charge

The electronic screening contribution can be computed with Eq. S3, which cannot be visualized easily due to the

separable part of the Hamiltonian (and its derivatives), which are nonlocal. On the other hand, one can express the electronic screening as [13]

$$\Delta Z_{\kappa,\beta\alpha} = 2 \frac{\Omega_0}{(2\pi)^3} \int_{\text{BZ}} \sum_m^{\text{occ}} s \left\langle u_{m\mathbf{k}}^{R_{\kappa\alpha}} | i u_{m\mathbf{k}}^{k_\beta} \right\rangle d\mathbf{k}, \quad (\text{S6})$$

where $u_{m\mathbf{k}}^{R_{\kappa\alpha}}$ is the derivative of the Bloch function with an atomic displacement, and $u_{m\mathbf{k}}^{k_\beta}$ is the derivative of the Bloch function with respect to the wave vector k_β . In the case of well-separated monolayers, and considering the electric field in the out-of-plane direction, this expression can be approximated in the real space as

$$\Delta Z_{\kappa,\beta\alpha} \approx \int_{\Omega_0} n_{R_{\kappa\alpha}}^{(1)}(\mathbf{r}) (r_\beta - R_{\kappa\beta}) d\mathbf{r}, \quad (\text{S7})$$

where $R_{\kappa\alpha}$ is the position of atom κ in the direction α and r_β is the spatial coordinate in direction β .

In what follows, we will focus on the displacement of the Mo (or Ti) atom of the upper plane of the unit cell in the out-of-plane direction. To simplify the following analysis, we perform an integration of Eq. (S7) over the \mathbf{a} and \mathbf{b} lattice vectors of MoS_2 . Eq. (S7) then becomes

$$\Delta Z_{\text{Mo},zz} \approx \int_{\mathbf{c}} (z - z_{\text{Mo}}) \tilde{n}_{\tau_{\kappa\alpha}}^{(1)}(z) dz, \quad (\text{S8})$$

where we have defined the planer integrated (a one-dimensional quantity) perturbed electronic density as $\tilde{n}_{\tau_{\kappa\alpha}}^{(1)}(z)$ which is simply the integrated electronic density in planes spanned by the \mathbf{a} and \mathbf{b} lattice vectors.

Bader Partitioned Dynamic Charge

As shown previously (Eq. S5), the BPDC depends on the Bader charge itself and its change with an atomic displacement. Defining the Bader volume $\Omega_{\kappa'}^B$ for the atom κ' , the Bader charge is simply given by

$$Z_{\kappa'}^B = Z_{\kappa'}^{\text{ion}} - \int_{\Omega_{\kappa'}^B} n^{(0)}(\mathbf{r}) d\mathbf{r}, \quad (\text{S9})$$

where $n^{(0)}(\mathbf{r})$ is calculated electron density. The derivative with respect to atomic position of Eq. (S9) is thus

$$\frac{\partial Z_{\kappa'}^B}{\partial R_{\kappa\alpha}} = - \int_{\Omega_{\kappa'}^B} n_{R_{\kappa\alpha}}^{(1)}(\mathbf{r}) d\mathbf{r} + F \left(\frac{\partial \Omega_{\kappa'}^B}{\partial R_{\kappa\alpha}} \right), \quad (\text{S10})$$

where we include first the integration of the perturbed electronic density over the Bader volume and the change of Bader volume with the atomic displacement. This last term cannot be easily represented in space, as discussed in what follows, and is not necessary for the qualitative explanation of the differences between the BPDC and the BEC. Therefore, we will ignore it in the remainder of the

discussion. By restricting ourselves to the displacement of Mo (or Ti) in the out-of-plane direction and performing the integration over \mathbf{a} and \mathbf{b} lattice vectors Eq. (S10) becomes

$$\frac{\partial Z_{\kappa'}^B}{\partial R_{Mo,z}} = - \int_{\tilde{z}_{\kappa'}} \tilde{n}_{R_{Mo,z}}^{(1)}(z) dz, \quad (S11)$$

where $\tilde{z}_{\kappa'}$ corresponds to the edge, in the z direction, of the Bader volume. The “full” dynamical contribution is obtained by summing over this last quantity, weighted by the atomic coordinate along z , as

$$\Delta Z_{Mo,z}^B = \sum_{\kappa'} \frac{\partial Z_{\kappa'}^B}{\partial R_{Mo,z}} R_{\kappa'z}. \quad (S12)$$

With the set of approximations presented here, both the dielectric screening contribution to the BEC and the dynamical contribution to the BPDC are expressed in terms of an integral over z of the linear perturbed electronic density weighted by a known factor. Their application to MoS_2 and TiS_2 are presented in the following subsection.

Analysis of the Dynamic Charges

This linear electronic density for MoS_2 and TiS_2 are shown in Fig. S7 alongside their corresponding ground state electronic density (plus core charge density) to give an idea of the range of the Bader volume. The contribution due to adjacent layers is negligible and not shown.

We first focus the discussion on MoS_2 . The dynamic contribution of the BPDC will be given, following Eq. S11, by the integration of the linear perturbed electronic density (red dotted curve) within the Bader volumes. The contribution within the Mo Bader volume vanishes as the linear perturbed electronic density is antisymmetric with respect to the Mo atom. Note that it corresponds to the null curvature of the Bader charge in Fig. S6 (c). The integration over the chalcogen Bader volumes (the red-filled area in Fig. S7) of the perturbed electronic density, however, will sum up when weighted by the atomic position, giving a net contribution to the BPDC. In contrast, the largest contribution to the BEC (blue solid curve) arises within the Bader volume of Mo (see Eq. S8 and Fig. S7) and is thus localized around the Mo atom.

Switching now to TiS_2 . One can see that the overall picture is different than shown for MoS_2 . Indeed, the largest contribution to the BEC arises from outside the Bader volume of Ti, while it was on contrary localized in the transition metal atomic region in MoS_2 . Concerning the dynamic contribution to the BPDC, the reasoning is similar to the case of MoS_2 , where it is found that the contribution within the Ti Bader volume is zero due

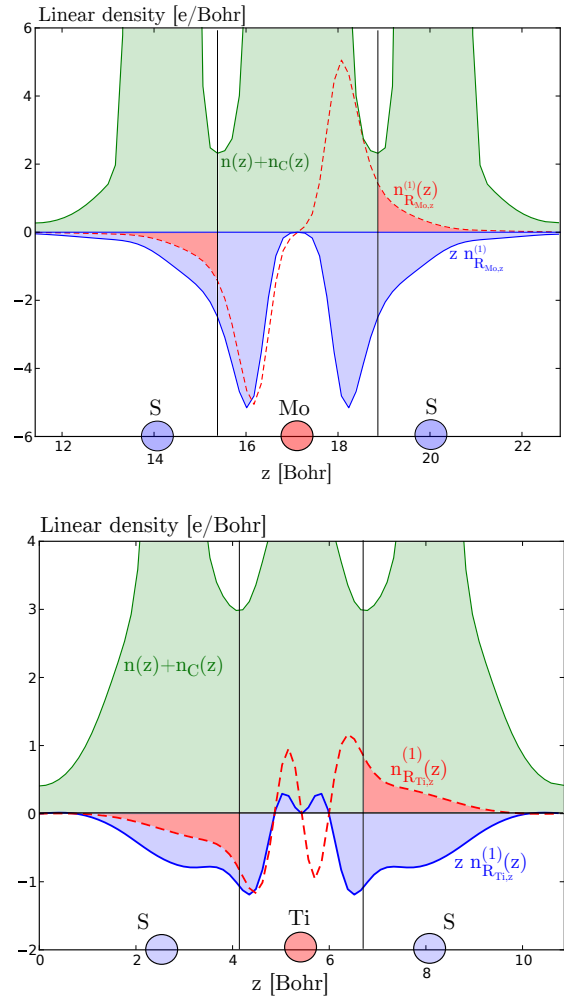


FIG. S7. (Color Online) In-plane-integrated electronic density (linear electronic density) as function as the out-of-plane (z) distance for (Top) bulk MoS_2 , (Bottom) bulk TiS_2 . Solid green is the sum of the ground state electronic density with the core-charge density. From the minima of this function, we extract the corresponding Bader volume range (solid vertical lines). In solid blue is the out-of-plane coordinate times the linear perturbed electronic density with respect to a displacement of the Mo atom in the out-of-plane direction, that gives, when integrated, an estimation of the dielectric screening contribution to the BEC. In dotted red is depicted the linear perturbed electronic density. Only the filled red area corresponds to the contribution of the BPDC.

to symmetry, and all the contributions come from the chalcogen Bader volumes.

With these analyses, we have a real-space picture of the origin of the counterintuitive sign of the BEC. Indeed, while most contributions to the Born effective charge come from outside the transition metal Bader volume in the case of TiS_2 , the contrary is observed for MoS_2 , with a well-localized response around the transition metal atom. This region cannot be properly described with the

Bader approach, as the net contribution to the BPDC is zero due to symmetry for that Bader volume. While it is not important in TiS_2 (most contribution to the dynamical charge comes from the chalcogen Bader volumes), it is, on the contrary, a large contribution in the case of MoS_2 referring to Fig. S7. As discussed by Ghosez and Gonze [11], while the BPDC would be able to describe charge localization/delocalization phenomena, it would fail to take into account any kind of local change in polarization. By the present analysis, we show that the sign of the BEC in MoS_2 is primarily due to this local change in polarization, while it plays little role in TiS_2 , for which the BPDC gives excellent agreement with the BEC. Quantifying such local polarization changes in MoS_2 requires the analysis of the electronic states close to the band gap. While the other electronic states are delocalized along the bonds, the last occupied band is an anti-bonding state, with electrons localized close to the Mo atoms, which explains the origin of the localized change of polarization.

ANALYSIS OF THE BAND-BY-BAND DECOMPOSITION OF THE BECS

The band-by-band decompositions of the BEC [18] in monolayer MoS_2 and bulk TiS_2 are shown in Table S2. The calculated BEC contributions of each band are clearly anomalous and show a large variation as a function of band index. When one sum ups over the bands for each charge (the quantity in the last row) one finds that the charge neutrality sum rule is fulfilled.

As mentioned in the main text, an evaluation of the band-by-band decomposition of the BEC and the localization tensor, which we do not show, is not helpful in deducing which bands, are specifically responsible for the anomalous net sign change.

EXPERIMENTAL CONFIRMATION

Finally, we propose in the main text that one can experimentally verify the sign of the BEC by measuring the angle-resolved Raman spectrum of the longitudinal optical mode as done in the work of Wolverson *et al* [19]. Here they state that the intensity of the Raman signal is related to the Raman tensor R whose components can be shown to be linearly related to the BEC of the material. To demonstrate this correspondence, we will first note that the intensity of the Raman signal, projected onto the plane of the sample and as a function of angle, θ , can be written as [19]

$$I(\theta) \propto u^2 \cos^2 \theta + w^2 \sin^2 \theta + v^2 + 2v(u+w) \sin \theta \cos \theta \quad (\text{S13})$$

and that the maximum and minimum values of the intensity are found at angles given when the first derivative

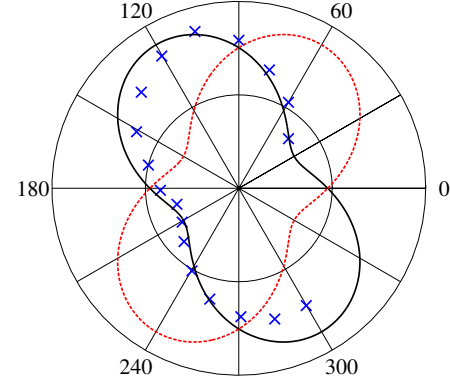


FIG. S8. (Color Online) Our calculated angle dependent Raman susceptibility, in black, using Eq. (S13) with experimental data points, blue x's, from Wolverson *et al.* [19]. The red line corresponds to the same calculation as the black curve, except we assumed that the sign of the BEC corresponds to the nominal charges in ReSe_2 .

of I is equal to zero. The result of this calculation gives the angle for the maximum and minimum values as:

$$\tan(2\theta) = \frac{2v}{u-w} \quad (\text{S14})$$

where, as we show below, u , v , and w are linearly dependent on the BEC.

From Veithen *et al.* [20] the Raman intensity, as a function of the scattering polarization, e_s (with scattering angle θ), is a sum over initial polarizations, e_i , of the form

$$I(\theta) \propto |e_s \cdot R^m \cdot e_i|^2 \propto |e_s \cdot \alpha^m \cdot e_i|^2 \quad (\text{S15})$$

which gives us the connection between the matrix elements of the Raman matrix R and the matrix elements of the Raman susceptibility α . Namely, $u = \alpha_{11}$, $v = \alpha_{12}$ and $w = \alpha_{22}$.

The Raman susceptibility tensor, α , is defined as [20]

$$\alpha_{ij}^m = \sqrt{V_0} \sum_{\kappa\beta} \frac{\partial \chi_{ij}^{(1)}}{\partial \tau_{\kappa\beta}} U_m(\kappa\beta) \quad (\text{S16})$$

which, for longitudinal optical phonons [20], is proportional to the BEC and can be written as:

$$\alpha_{ij}^m \propto X_{ij} - \sum_l Z_{ml}^* q_l \times \frac{\sum_l \chi_{ijl}^{(2)} q_l}{\sum_{l,l'} q_l \epsilon_{l,l'} q_{l'}} \quad (\text{S17})$$

where $Z_{ml}^* = \sum_{\kappa\beta} U_m(\kappa\beta) Z_{\kappa\beta l}^*$ is a mode dipole vector, ϵ is the dielectric tensor, q_l is the phonon unit vector in the l^{th} direction, and $X_{ij} = \sum_{\kappa\beta} \frac{\partial \chi_{ij}^{(1)}}{\partial \tau_{\kappa\beta}} \Big|_{\epsilon_0=0}$ is the derivative of the component of the linear dielectric susceptibility.

Band	MoS ₂				TiS ₂			
	Mo _{xx}	Mo _{zz}	S _{xx}	S _{zz}	Ti _{xx}	Ti _{zz}	S _{xx}	S _{zz}
Z _{ion}	6.00	6.00	6.00	6.00	4.00	4.00	6.00	6.00
1	0.05	-23.12	-1.02	10.57	-0.42	-36.74	-0.78	17.38
2	0.18	23.49	-1.09	-12.75	0.63	36.78	-1.32	-19.40
3	-1.19	-13.55	-0.28	5.78	8.97	-28.37	-5.49	13.10
4	0.13	4.05	-0.89	-3.03	-7.96	18.89	3.15	-10.28
5	4.67	3.75	-3.72	-2.87	1.66	-6.59	-1.83	2.37
6	-6.16	-11.19	2.32	4.60	-7.40	-11.17	2.71	4.37
7	-5.03	12.79	1.77	-7.40	0.38	22.66	-1.00	-12.05
8	121.05	7.24	-63.13	-4.62	6.45	1.74	-4.60	-2.09
9	-120.80	-9.52	60.58	3.76				
Tot.	-1.10	-0.07	0.55	0.04	6.30	1.21	-3.15	-0.60

TABLE S2. Band-by-band decomposition of the BEC of monolayer MoS₂ and bulk TiS₂ where the line Z_{ion} gives the ionic charge of the pseudopotential. The total number of calculated bands for each case depends on the ionic charge of the pseudopotential.

For bulk compounds such as the h-TMDs and the t-TMDs one can evaluate Eq. (S17) and determine that the symmetry of the crystal structure prevents one from observing the Raman susceptibility since the second-order non-linear optical susceptibility, $\chi_{ij}^{(2)}$, is zero and the Raman susceptibility is diagonal ($v = 0$). However in compounds with reduced symmetry, such as ReSe₂, the second-order non-linear optical susceptibility is non-zero [21]. We have calculated the Raman susceptibility and second-order nonlinear optical susceptibility in bulk ReSe₂ and found that they are non-zero and in agreement with the calculated and measured values of Wolverson *et al.* [19].

In Fig. S8 we plot the polarization intensity as a function of angle for our calculations of the Raman susceptibility tensor (black line) for the longitudinal optical mode of ReSe₂, the experimental data points from Wolverson *et al.* [19] in blue X's, and the red line is our calculation assuming the sign of the BEC on the transition metal and chalcogen are reversed (and thus in agreement with the Bader static charge). Our calculation of the Raman susceptibility tensor with opposite BECs assumes the remaining quantities used to calculate Eq. (S17) remain unchanged.

Pu.” J. Chem. Phys. **132**, 154104 (2010).

- [4] X. Gonze, B. Amadon, P. M. Anglade, J.-M. Beuken, F. Bottin, P. Boulanger, F. Bruneval, D. Caliste, R. Caracas, M. Cote, T. Deutsch, L. Genovese, Ph. Ghosez, M. Giantomassi, S. Goedecker, D. Hamann, P. Hermet, F. Jollet, G. Jomard, S. Leroux, M. Mancini, S. Mazevedt, M.J.T. Oliveira, G. Onida, Y. Pouillon, T. Rangel, G.-M. Rignanese, D. Sangalli, R. Shaltaf, M. Torrent, M.J. Verstraete, G. Zérah, and J.W. Zwanziger. “ABINIT : first-principles approach to material and nanosystem properties.” Comput. Phys. Commun. **180**, 2582-2615 (2009).
- [5] R. Dickinson and L. Pauling. “The crystal Structure of Molybdenite.” J. Amer. Chem. Soc. **45**, 1466-1471 (1923).
- [6] L. H. Brixner. “Preparation and properties of the single crystalline AB₂-type selenides and tellurides of niobium, tantalum, molybdenum and tungsten.” J. Inorg. Nucl. Chem. **24**, (1962).
- [7] A. Berkdemir, H. R. Guiterrez, A. R. Botello-Mendez, N. Perea-Lopez, A. L. Elias, C.-I. Chia, V. H. Crespi, F. Lopez-Urias, J-C. Charlier, H. Terrones, and M. Terrones. “Identification of individual and few layers of WS₂ using Raman Spectroscopy.” Sci. Repts. **3**, 1755 (2013).
- [8] M. Traving, M. Boehme, L. Kipp, M. Skibowski, F. Starost, E. E. Krosovskii, A. Perlov, and W. Schattke. “Electronic Structure of WSe₂: A combined photoemission and inverse photoemission study.” Phys. Rev. B **55**, 10392 (1997).
- [9] C. Wan, Y. Wang, N. Wang, and K. Koumoto. “Low-Thermal-Conductivity (MS)_{1+x}(TiS₂)₂ (M = Pb, Bi, Sn) Misfit layer Compounds for Bulk Thermoelectrics.” Materials **3**, (2010).
- [10] P. Chen, Y-H. Chan, X-Y. Fang, Y. Zhang, M. Y. Chou, S-K. Mo, Z. Hussain, A. V. Fedorov, and T. C. Chaing. “Charge density wave transition in single-layer titanium diselenide. Nature Communications. **6**, 8943 (2015).
- [11] Ph. Ghosez, J-P. Michenaud, and X. Gonze. “Dynamical atomic charges: The case of ABO₃ compounds.” Phys. Rev. B **58**, 6224 (1998).
- [12] A. Kokalj, “Computer graphics and graphical user interface as tools in simulations of matter at the atomic scale.” Comp. Mat. Sci. **28**, 155 (2003).
- [13] X. Gonze and C. Lee. “Dynamical matrices, Born effective charges, dielectric permittivity tensors, and, inter-

* Co-first author; Nicholas.pike@ulg.ac.be

† Co-first author

- [1] J. P. Perdew, K. Burke, and M. Ernzerhof, “Generalized Gradient Approximation Made Simple.” Phys. Rev. Lett. **77**, 2865 (1996).
- [2] M. Fuchs and M. Scheffler. “Ab initio pseudopotentials for electronic structure calculations of poly-atomic systems using density-functional theory.” Comput. Phys. Commun. **119**, 67 (1999).
- [3] S. Grimme, S. Ehrlich, and L. Goerigk. “A consistent and accurate ab initio parametrization of density functional dispersion correction (DFT-D) for the 94 elements H-

atomic force constants from density-functional perturbation theory.” *Phys. Rev. B* **55**, 10355 (1997).

[14] P. E. Blochl. “Projected augmented-wave method.” *Phys. Rev. B* **50**, 17953 (1994).

[15] M. Torrent, F. Jollet, F. Bottin, G. Zérah and X. Gonze, “Implementation of the projector augmented-wave method in the ABINIT code: Application to the study of iron under pressure.”, *Comput. Mater. Sci.* **42**, 337-351 (2008).

[16] F. Jollet, M. Torrent and N. Holzwarth. “Generation of Projected Augmented-Wave atomic data: A 71 element validated table in XML format.” *Comp. Phys. Commun.* **185**, 1246-1254 (2014).

[17] M. A.L. Marques, M. J.T. Oliveira and T. Burnus. “Libxc: A library of exchange and correlation functionals for density functional theory.” *Comp. Phys. Commun.* **183**, 2272-2281 (2012).

[18] M. Veithen, X. Gonze, and Ph. Ghosez, ”Electron localization: Band-by-band decomposition and application to oxides.” *Phys. Rev. B*, **66**, 253113 (2002).

[19] D. Wolverson, S. Crampin, and A. S. Kazemi, and A. Ilie and S. J. Bending. “Raman Spectra of Monolayer, Few-Layer and Bulk ReSe₂: An Anisotropic Layered Semiconductor.” *ACS Nano* **8**, 11154-11164 (2014).

[20] M. Veithen, X. Gonze, and Ph. Ghosez. “Non-linear optical susceptibilities, Raman efficiencies and electrooptic tensors from first-principles density functional perturbation theory.” *Phys. Rev. B* **71**, 125107 (2005).

[21] N. Kumar, S. Najmaei, Q. Cui, F. Ceballos, P. M. Ajayan, J. Lou, and H. Zhao. “Second Harmonic microscopy of monolayer MoS₂.” *Phys. Rev. B* **87**, 161403(R) (2013).